Journal of Magnetism and Magnetic Materials 559 (2022) 169530

Contents lists available at ScienceDirect

Journal of Magnetism and Magnetic Materials

journal homepage: www.elsevier.com/locate/jmmm

Enhancement of ferromagnetism and ferroelectricity by oxygen vacancies in mullite $Bi_2Fe_4O_9$ in the $Bi_2(Sn_{0.7}Fe_{0.3})_2O_{7-x}$ matrix

S.S. Aplesnin [a,b], L.V. Udod [a,b,*], M.N. Sitnikov [b], D.A. Velikanov [a], M.N. Molokeev [a], O.B. Romanova [a], A.V. Shabanov [a]

[a] Kirensky Institute of Physics, Federal Research Center KSC SB RAS, 660036 Krasnoyarsk, Russia
[b] Reshetnev Siberian State University of Science and Technology, 660037 Krasnoyarsk, Russia

ARTICLE INFO

Keywords:
Remanent magnetization
Remanent polarization
Magnetic hysteresis
Electrical hysteresis
Impedance
Permittivity

ABSTRACT

A new bismuth pyrostannate-based composite $Bi_2(Sn_{0.7}Fe_{0.3})_2O_{7-x}/Bi_2Fe_4O_9$ (BSFO/BFO) has been obtained by the solid-state synthesis. Temperature dependences of the magnetic hysteresis and remanent magnetization and the nonlinear field dependence of the magnetization for the $Bi_2Fe_4O_9$ antiferromagnet have been established. A temperature of the formation of canted sublattices in the antiferromagnet with the occurrence of a spontaneous moment in mullite has been determined. The mechanism of the electric polarization hysteresis and the temperature dependence of the remanent polarization have been established. It has been shown, that, below the Néel temperature, the dipole polarization is induced by a lone electron pair of bismuth ions. At $T > T_N$, the migration polarization is caused by the charge carrier density at the chemical potential. A significant increase in the remanent magnetization of mullite in the bismuth pyrostannate matrix with oxygen vacancies over a value typical of polycrystalline mullite has been established. Remanent magnetization is explained in terms of ferron model.

1. Introduction

Mullite $Bi_2Fe_4O_9$ is a multifunctional material, which is used in chemical industry and promising for microelectronics. The mullite-type materials $Bi_2M_4O_9$ ($M = Al^{3+}$, Ga^{3+}, Fe^{3+}) are highly sensitive to acetone and ethanol vapors and find application in semiconductor gas sensors [1] and photocatalytic oxidation [2,3], owing to their narrow bandgap, and in fuel cell electrolytes due to their high ionic conductivity [4]. The $Bi_2Fe_4O_9$ compound is exploited as a high-performance catalyst [5] and in sensing and digital memory [6]. Bismuth ferrite $Bi_2Fe_4O_9$ is used as a catalyst for oxidation of ammonia to NO in the commercial production of nitric acid [2].

The multiferroic materials, which exhibit the ferroelectric (FE) and ferromagnetic (FM) properties simultaneously, including composites with magnetoelectric coupling are widely used in spintronics [7]. In particular, the $Bi_{3.15}Nd_{0.85}Ti_3O_{12}$ ferroelectric film includes the $CoFe_2O_4$ ferromagnetic regions and exhibits the magnetoelectric interaction [8]. The $PbZr_{0.53}Ti_{0.47}O_3)_{(1-x)}$–$(PbFe_{0.5}Ta_{0.5}O_3)_x$ composite has the ferroelectric and magnetic properties with a linear magnetoelectric effect at room temperature [9]. The magnetoelectric parameters of the composite multiferroics are superior to those of single-phase systems by two–three orders of magnitude [10,11].

Bismuth pyrostannate $Bi_2Sn_2O_7$ is an insulator. Its magnetic and electrical properties can be controlled via the cationic substitution of 3d elements. The heterovalent substitution of Cr^{3+} ions for Sn^{4+} ones in $Bi_2Sn_2O_7$ evokes the dipole glass state, electron polarization, and its hysteresis [12,13]. The paramagnetic Curie temperature of the $Bi_2(Sn_{0.95}Cr_{0.05})_2O_7$ compound in the range of $0 < T < 40$ K is $\theta \approx 2$ K. The inverse susceptibility of $Bi_2(Sn_{0.9}Cr_{0.1})_2O_7$ has an inflection point in the region of the $\alpha \rightarrow \beta$ transition at $T = 370$ K [14]. As the chromium ion concentration increases, the paramagnetic Curie temperature rises to $\theta = 180$ K [15].

Substitution of iron ions in bismuth pyrostannate $Bi_2(Sn_{1-x}Fe_x)_2O_7$ ($x = 0.1, 0.2$) changes the sign of the exchange coupling. According to the Mössbauer and electron spin resonance studies, iron ions occupy two nonequivalent octahedral sites in the pyrochlore crystal structure and are in the high-spin state. The temperature dependences of the magnetic susceptibility of the $Bi_2(Sn_{1-x}Fe_x)_2O_7$ ($x = 0.1, 0.2$) compound measured in a magnetic field of 600 Oe are typical of paramagnets. The paramagnetic Curie temperature sharply increases from $\theta = -10$ K at $\times = 0.1$

* Corresponding author at: Kirensky Institute of Physics, Federal Research Center KSC SB RAS, 660036 Krasnoyarsk, Russia.
E-mail address: luba@iph.krasn.ru (L.V. Udod).

https://doi.org/10.1016/j.jmmm.2022.169530
Received 29 December 2021; Received in revised form 29 March 2022; Accepted 23 May 2022
Available online 30 May 2022

to θ_1 = -39.2 K at × = 0.2 with an increase in the iron concentration. At × = 0.2, a decrease in the magnetic moment and antiferromagnetic exchange in the region of the structural phase transition from a triclinic to monoclinic structure at T = 140 K was found. The nonlinear behavior of the magnetization in magnetic fields of up to 50 kOe in the paramagnetic state at temperatures of up to 200 K is attributed to the magnetoelectric interaction. The magnetic field-induced electric polarization is an even function of the magnetic field, except for the region 140–160 K of the structural phase transition, where the linear magnetoelectric effect prevails [16,17].

Mullite $Bi_2Fe_4O_9$ is described by a centrosymmetric sp. gr. *Pbam*. The $Bi_2Fe_4O_9$ crystal lattice consists of FeO_6 octahedra coupled with Fe_2O_7 double tetrahedra. The Fe^{3+} ions occupy two different sites: octahedral and tetrahedral [18,20]. At T = 264 ± 3 K, the bulk $Bi_2Fe_4O_9$ compound passes to the antiferromagnetic state. The magnetic moment on Fe^{3+} ions is μ_B = 4.95 μ_B [20] or, according to other data, μ_B = 3.9–4.0 μ_B [21]. The magnetic properties of polycrystalline bismuth ferrite $Bi_2Fe_4O_9$ depend on a synthesis method used and a crystallite size. At room temperature, the sample with a grain size of 200–450 nm synthesized using ethylene diamine tetra acetic acid behaves like a weak ferromagnet [22]. The $Bi_2Fe_4O_9$ sample with micron grains obtained by melting exhibits the magnetization hysteresis and undergoes a magnetic phase transition at 250 K [23,24]. Polycrystalline ceramics $Bi_2Fe_4O_9$ with grains smaller than 200 nm is characterized by magnetic hysteresis at the room-temperature, which vanishes upon heating [25]. The $Bi_2Fe_4O_9$ samples obtained by the solid-state synthesis have a Néel temperature of T_N = 258 K [26] and T_N = 238 K in the single-crystal state [19]. A critical grain size of 50 nm corresponding to the occurrence of magnetization hysteresis at the room-temperature was found in the $Bi_2Fe_4O_9$ compound synthesized by glycine combustion [27]. The change in the slope of the temperature dependence of the permittivity and the maximum dissipation factor near the Néel temperature were explained by the magnetoelectric interaction [28].

Despite the great amount of the available data on the magnetic properties of the $Bi_2Fe_4O_9$ compound, the temperature dependence of the M(H) hysteresis for this composite remains unexplored. The hysteresis exists above the Néel temperature in the polycrystals with a subcritical grain size and is explained by the uncompensated sublattices magnetic moments. In the paramagnetic state, only a short-range order exists, which cannot cause the hysteresis and residual magnetic moment.

In antiferromagnetic semiconductors, the creation of magnetization due to impurity electrons is possible. Oxygen vacancies near iron ions in octahedra lead to a change in the energy of the spin crossover from a low-spin state to a high-spin state, the appearance of metastable magnetic states with spin 0 and 4 μ_B/cell for Fe [29] The type of oxygen vacancies from V_O^+ to V_O^{2+} in $Ti_{1-\delta}Mn(II)_\delta O_2$ changes the sign of the exchange interaction from negative to positive (ferromagnetic) according to calculations in the Hybrid functional model [30]. In $SrNiO_{3-\delta}$ perovskites with an oxygen deficiency δ up to 0.375 using density functional theory, the magnetic moment on vacancies d^8 L^2 and d^7 L was calculated, which leads to a decrease in the net magnetization [31]. A similar effect was found in the double perovskite Sr_2FeMoO_6 [32].

Oxygen-vacancy induced magnetic phase transitions in multiferroic as a results of restore missing magnetic super-exchange interactions in large axial ratio phases, leading to full antiferromagnetic spin ordering, and induce the stabilization of ferrimagnetic states with considerable net magnetizations [33].

Non-stoichiometric substitution changes the degree of doping of the semiconductor; it is possible to control not only its electrical but also magnetic properties, for example, at high concentration of doping, the initial antiferromagnetic ordering can be replaced by a ferromagnetic one. An individual electron can create a ferromagnetic microregion and self-localize in it, forming a ferron. The losses of energy for the flip of localized spins are compensated by the gain in electron energy, since the microregion is a potential well for an electron in an antiferromagnetic crystal. Ferron can move through the crystal and dissociates with increasing temperature. The dissociation temperature can exceed the Néel temperature [34]. The radius of the ferrons increases at the heating and the formation of the net magnetization is possible as a result of the interaction between electrons captured by oxygen vacancies [35].

The electric polarization hysteresis is observed also in the polycrystalline samples and depends on a synthesis technique and a type of 3d substituents used. It is assumed that ferroelectricity is caused by a lone electron pair of bismuth ions and, at room temperature, has a dipole nature. Then, the polarization should decrease upon heating and vanish at the critical temperature.

Pyrochlore compounds have nominal composition $A_2B_2O_7$, and their structure consists of two interpenetrating B_2O_6 octahedral and A_2O' tetrahedral networks. The predisposition to oxygen nonstoichiometry in pyrochlores can be rationalized by considering the structure to exist as two interpenetrating B_2O_6 and A_2O' networks. The stoichiometry of pyrochlore compounds is often expressed as $A_2B_2O_6O'$, denoting the existence of two distinguishable oxygen sites. Within the pyrochlore structure, there is only a weak interaction between the two networks, and the A_2O' tetrahedral substructure has a minor contribution to the Madelung energy, which enables the synthesis of nonstoichiometric pyrochlore compounds. The diffraction data for $Pb_2Ir_2O_{6.5}$ have been used to refine the structure in the cubic space group $F\bar{4}3m$, in which there is oxygen vacancy ordering and where each Pb atom is displaced 0.04 Å toward its associated vacancy. For $Bi_2Ir_2O_{7-y}$ the structure was fitted within space group Fd3m, in which the oxygen vacancies are randomly distributed over the O' sites. In both structures the Ir atoms are in a nearly regular octahedral coordination whereas the Bi and Pb cations have a distorted eightfold coordination, compressed scalehedron, geometry [36].

We suppose that, at room temperature, the electric polarization is related to the oxygen vacancies, which induce the electron migration polarization. Oxygen defects cause the formation of a divalent state of iron ions. Via creating oxygen vacancies artificially, one can improve the ferromagnetic and ferroelectric characteristics. To do that, the $Bi_2(Sn_{0.7}Fe_{0.3})_2O_{7-x}/Bi_2Fe_4O_9$ (BSFO/BFO) composite was synthesized, in which bismuth pyrostannate contains ~ 4% of oxygen vacancies. The aim of the study was to improve the ferromagnetic and ferroelectric properties of mullite $Bi_2Fe_4O_9$.

2. Materials and methods

The BSFO/BFO composite was synthesized by the solid-state reaction method according to the scheme:

$2(1–0.3)SnO_2 + 0.3Fe_2O_3 + Bi_2O_3 \rightarrow Bi_2(Sn_{0.7}Fe_{0.3})_2O_{7-x}$ - $Bi_2Fe_4O_9$.

The initial reagents were fine powders of oxides Bi_2O_3, SnO_2, and Fe_2O_3. The stoichiometric mixture of the initial components was thoroughly ground in an agate mortar with ethyl alcohol until a homogeneous state. The charge was pressed at room temperature and annealed at 800–950 °C in several stages.

The morphology, energy-dispersive X-ray spectroscopy (EDS) and selected area electron.

diffraction (SAED) investigations of the samples were carried out on a Hitachi S5500 scanning electron microscope (SEM). Scanning performed in different microregions of the samples yielded identical results. To obtain an electron diffraction pattern, the surface of the sample was etched with argon.

The magnetic properties of the samples were examined on an MPMS-XL Magnetic Property Measurement System in the temperature range of 4–275 K in two modes. In the zero-field cooling (ZFC) mode, the sample was cooled to the liquid helium temperature in zero magnetic field; after that, a magnetic field of H = 600 Oe was applied and the magnetic moment of the sample was measured upon heating of the latter. In the field cooling (FC) mode, the sample was cooled in a magnetic field of 50 000 Oe and then the magnetic moment was measured in a magnetic field

of 600 Oe. The capacitance and dissipation factor were measured on an AM-3028 component analyzer in the frequency range of 1–300 kHz at temperatures of 80–500 K. The field dependence of the electric polarization P(E) was determined using the relation P = ∫jdt by measuring the current in a quasi-periodic field with a frequency of ω = 0.01 Hz. Three measurement cycles were performed on the samples with copper contacts formed.

3. Results and discussion

3.1. Characterization

According to the X-ray diffraction data, the synthesized composite consists of $Bi_2(Sn_{0.7}Fe_{0.3})_2O_{7-x}$ (91%) and $Bi_2Fe_4O_9$ (9%). The X-ray powder diffraction pattern was taken on a Bruker D8 ADVANCE diffractometer at room temperature. In the experiment, a VANTEC linear detector (Cu-Kα radiation) was used. Bismuth pyrostannate $Bi_2(Sn_{0.7}Fe_{0.3})_2O_{7-x}$ corresponds to the monoclinic *Pc* cell of the $Bi_2Sn_2O_7$ α- phase [37] and to the orthorhombic structure *Pbam* of $Bi_2Fe_4O_9$ [38] In the Rietveld refinement of the structure, the initial structures of these phases were used. The refinement was made in the TOPAS 4.2 program [39] and yielded low unreliability factors R (see Table 1 and Fig. 1).

The $Bi_2Sn_2O_7$ crystal structure contains 32 Bi^{3+} ions, 32 Sn^{4+} ions, and 112 O^{2-} ions in the independent part of the cell (Fig. 2a). All Bi^{3+} ions have eight O^{2-} ions in the nearest environment and form distorted cubes, while Sn^{4+} ions are surrounded by six O^{2-} ions and form vertex-sharing octahedra.

The $Bi_2Fe_4O_9$ crystal lattice consists of FeO_6 octahedra oriented parallel to the *c* axis and coupled with Fe_2O_7 double tetrahedra (Fig. 2b) [19] Bi^{3+} ions are surrounded by eight oxygen ions with the mutually orthogonal short BiO_3 bonds and longer BiO_5 bonds [38].

SEM images in Fig. 3a show the morphologies of the BSFO/BFO samples etched with argon. The analysis of the BSFO/BFO SEM images allowed us to establish the size distribution of $Bi_2Fe_4O_9$ grains in the $Bi_2(Sn_{0.7}Fe_{0.3})_2O_{7-x}$ matrix. In Fig. 3a, $Bi_2Fe_4O_9$ grains in the form of dark truncated plates with irregular edges are highlighted. A similar shape of the plates was observed for the $Bi_2Fe_4O_9$ synthesized by the hydrothermal method [40]. The selected area electron diffraction (SAED) pattern exhibits the highly crystalline nature of the particles and the indexing of the lines corresponds to the orthorhombic $Bi_2Fe_4O_9$ structure (Fig. 3b).

The grain size distribution is shown in Fig. 4. The average grain size was found to be 0.65–1.0 μm.

The EDS study confirmed the BSFO/BFO chemical composition (Fig. 5). The observed elemental compositions of the Bi, Sn, Fe, and O for $Bi_2(Sn_{0.7}Fe_{0.3})_2O_{7-x}$ phases (Fig. 5a) and the Bi, Fe, and O for $Bi_2Fe_4O_9$ phases (Fig. 5b) are indicative on the high quality of the samples and the oxygen content lower than for stereochemical composition. The increase of the iron ions intensity for mullite, in comparison with stannate, is confirmed by the calculated values weight percentages (5 wt% in stannate, and 28 wt% in mullite).

Table 1
Structural parameters of the BSFO/BFO composite.

	$Bi_2(Sn_{0.7}Fe_{0.3})_2O_{7-x}$	$Bi_2Fe_4O_9$
Sp. gr.	*Pc*	*Pbam*
a, Å	15.0927 (5)	7.96795 (2)
b, Å	15.0830 (5)	8.45160 (3)
c, Å	21.3150 (8)	6.01100 (2)
β, °	89.931 (2)	90 (2)
V, Å^3	4852.2 (3)	404.792661 (3)
2θ range,°	5–90	
R_{wp}, %	9.06	
R_p, %	7.01	
R_B, %	3.01	
χ^2	1.61	

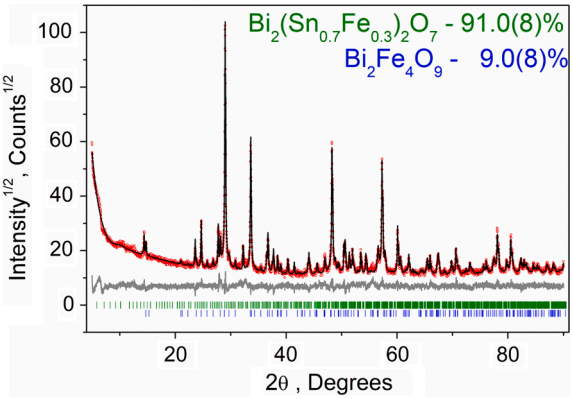

Fig. 1. Difference XRD pattern of the BSFO/BFO. The upper curve shows the experimental XRD pattern; the middle curve, the theoretical XRD pattern; and the lower curve, the difference between the theoretical and experimental XRD patterns. The phases of the BSFO/BFO marked by color: $Bi_2(Sn_{0.7}Fe_{0.3})_2O_7$ is green and $Bi_2Fe_4O_9$ is blue. (For interpretation of the references to color in this figure legend, the reader is referred to the web version of this article.)

3.2. Magnetic properties

The temperature dependence of the magnetic susceptibility of the BSFO/BFO composite measured in the ZFC mode and in a magnetic field of H = 600 Oe have anomalies in the temperature ranges of 30–40 K and 225–235 K (Fig. 6). The temperature dependence of the inverse magnetic susceptibility is nonlinear and does not obey the Curie-Weiss law over the entire temperature range. In the ZFC curve, the 1/χ nonlinearity weakens. At a temperature of 5 K, the polycrystalline $Bi_2Fe_4O_9$ compound is a weak ferromagnet with canting of the magnetic moments of iron ions in the antiferromagnetic lattice [23]. The χ (T) anomaly at 225–235 K is caused by the magnetic phase transition of the $Bi_2Fe_4O_9$ compound from the antiferromagnetic to paramagnetic state.

Upon cooling in a strong magnetic field (H = 50 kOe), the weak ferromagnetic moments M_r of crystallites orient along the field. The paramagnetic contribution to the susceptibility is made by structural defects ($\chi_1 = C_1/T$) and bismuth stannate ($\chi_2 = C_2/(T - \theta)$). The resulting susceptibility of the BSFO/BFO composite is described by a fitting function with three parameters: the Curie temperature ϑ and the Curie-Weiss constants C_1 and C_2:

$$\chi = (1-x)\chi_2 + \chi_1 + \frac{xM_r}{H} = \frac{(1-x)C_2}{T-\theta} + \frac{C_1}{T} + \frac{xM_r}{H} \quad (1)$$

where × is the mullite concentration and $C_{1,2}$ are the Curie-Weiss constants, $C_1 = 3.06 \cdot 10^{-4}$ and $C_2 = 5.54 \cdot 10^{-3}$ cm^3/K·mol. We determine the remanence magnetization from the M(H) curves. Fitting function (1) satisfactorily describes the experiment. The ZFC magnetic susceptibility of the sample is lower by ~ 40% due to the absence of remanent magnetization. The experimental data are described by only the paramagnetic contribution:

$$\chi = (1-x)\chi_2 + \chi_1 = \frac{(1-x)C_2}{T-\theta} + \frac{C_1}{T} \quad (2)$$

where a paramagnetic Curie temperature of θ = -50 K. The paramagnetic Curie temperature of the $Bi_2(Sn_{1-x}Fe_x)_2O_7$ sample monotonically grows with an increase in the concentration from θ = -10 K for × = 0.1 to θ = -39 K for × = 0.2 K.

Fig. 7 shows the field dependence of the magnetization, which is hysteretic at all temperatures. The hysteresis is symmetric about axes. The M(H) dependence for the BSFO/BFO composite is convex and qualitatively differs from the field dependence of the magnetization of an antiferromagnet. Upon heating to T = 100 K, the remanent

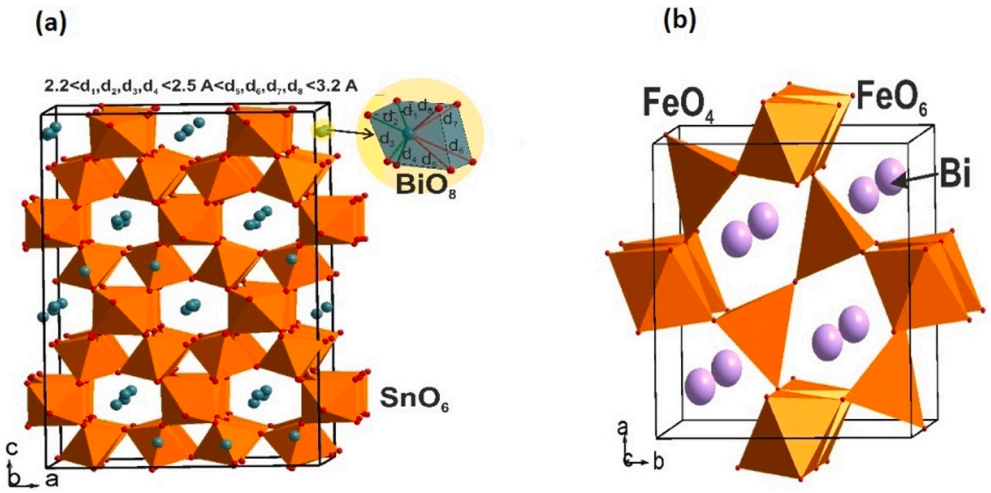

Fig. 2. The crystal structure. a) The crystal structure of the $Bi_2(Sn_{0.7}Fe_{0.3})_2O_{7-x}$. The BiO_8 fragment is shown separately. Bond lengths are indicated, d_{1-4} take values in the range 2.2–2.5 Å, and bond lengths d_{5-8}, respectively, 2.5–3.2 Å. b) The crystal structure of the $Bi_2Fe_4O_9$.

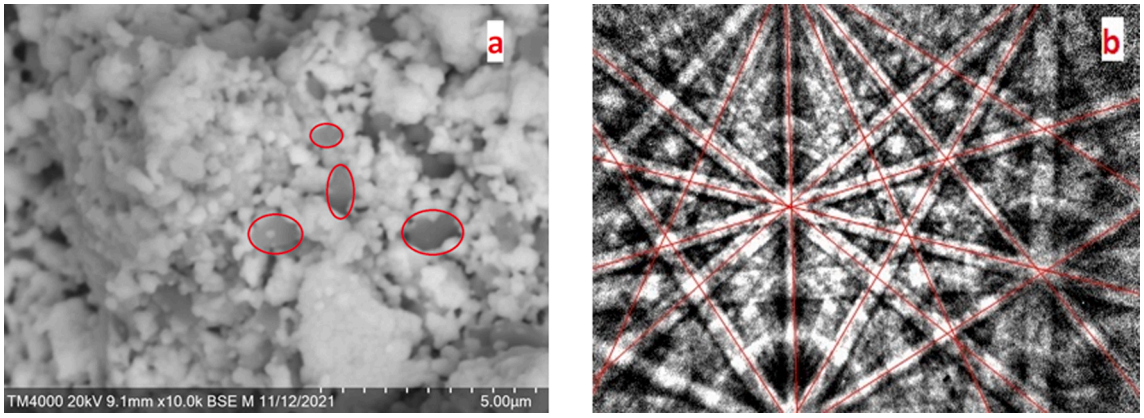

Fig. 3. SEM image of BSFO/BFO (a). Highlighted dark areas correspond to $Bi_2Fe_4O_9$. SAED of $Bi_2Fe_4O_9$ (b).

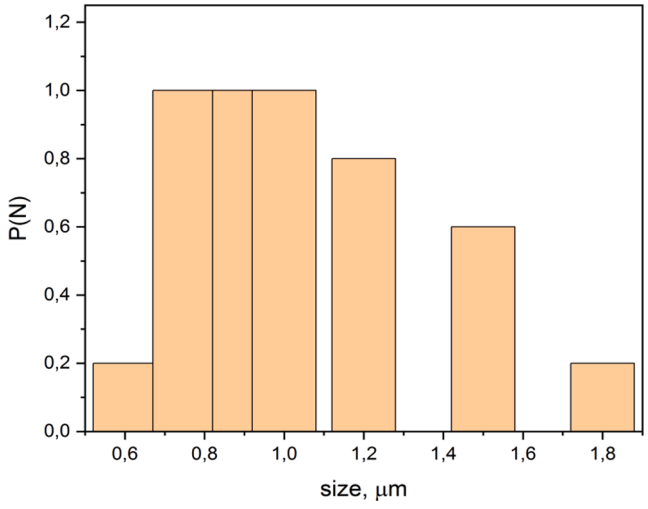

Fig. 4. The grain size distribution function of $Bi_2Fe_4O_9$.

magnetization decreases by a factor of 4 and then increases by a factor of 6. At a temperature of T = 5 K, the remanent magnetization is M_r = 0.017 emu/g; at T = 273 K, M_r = 0.024 emu/g; and its minimum value is M_r = 0.0038 emu/g [41]. Upon heating, the coercivity increases from 200 Oe at T = 100 K to 2000 Oe at T = 273 K.

The formation of the magnetic hysteresis is described within several available models. In the polycrystalline $Bi_2Fe_4O_9$ compound with a grain size of smaller than 5 nm, the ferromagnetic moment is explained by an increase in the uncompensated moment upon cell deformation or with an increase in the number of oxygen vacancies, which break the exchange couplings. In a field of H = 2 T, the maximum magnetization and coercivity increase from 0.144 μ_B/f.u. to 0.202 μ_B/f.u. with a decrease in the nanoparticle size from 50 to 5 nm. The number of uncompensated spins on the grain surface will increase with decreasing particle size [42]. The formation of the hysteresis depends not only on the particle size, but also on a synthesis technique used. At room temperature, the hysteresis loops are observed in ceramics with a grain size of 60–2000 nm obtained by the Pechini method [25]. In the polycrystals with a grain size of 50–750 nm synthesized by glycine combustion, a critical grain size of 750 nm was found, at which the sample becomes paramagnetic [27]. The nanoplate-shaped $Bi_2Fe_4O_9$ samples synthesized by the hydrothermal method at T = 270° C exhibit the hysteresis only in the low-temperature region (at T = 5 K) [32]. In bismuth pyrostannate $Bi_2(Sn_{1-x}Fe_x)_2O_7$ (x = 0.1, 0.2), the M(H) hysteresis was not observed [16]. The M(H) hysteresis observed for the BSFO/BFO compound over the entire temperature range is induced by $Bi_2Fe_4O_9$.

The magnetic hysteresis of $Bi_2Fe_4O_9$ was studied at room temperature and at T = 5 K. The absence of the temperature dependence of the remanent magnetization caused the incorrect explanation by the uncompensated magnetization of the sublattices in microsclusters with the broken exchange couplings. In this case, the sublattice magnetization

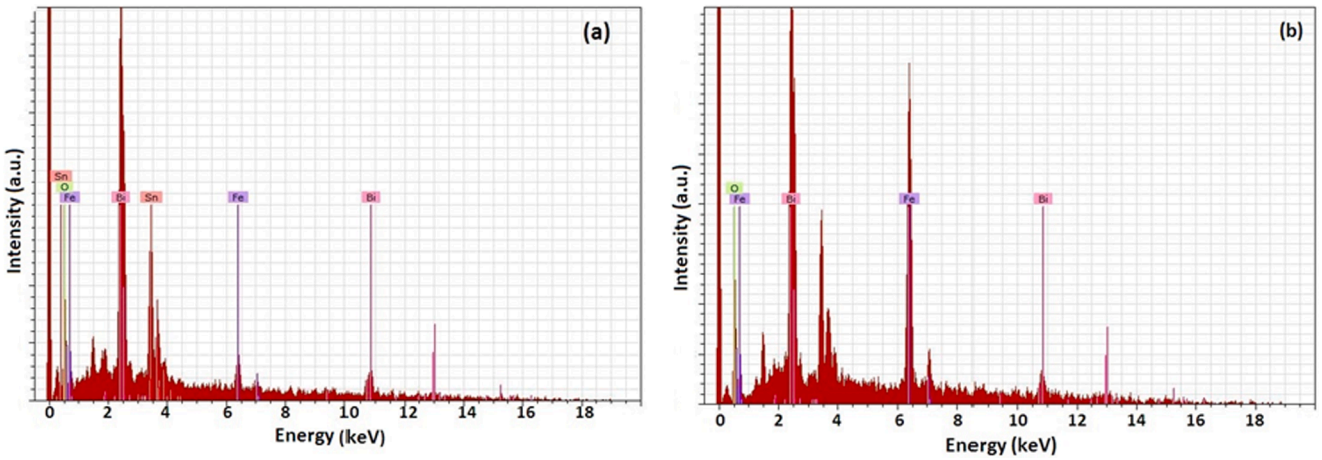

Fig. 5. EDS of (a) $Bi_2(Sn_{0.7}Fe_{0.3})_2O_{7-x}$ and (b) $Bi_2Fe_4O_9$.

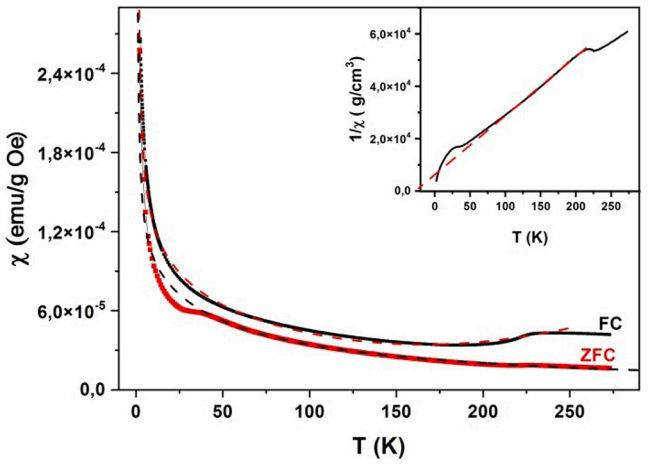

Fig. 6. The temperature dependence of magnetic susceptibility of BSFO/BFO. Dashed lines corresponds to theoretical calculations of expressions (1) and (2). Inset corresponds to the temperature dependence of the inverse susceptibility of BSFO/BFO.

decreases upon heating according to a power law. Our investigations shown the sharp $M_r(T)$ grows upon approaching the temperature of the magnetic phase transition. In addition, the hysteresis is observed above the Néel temperature in the paramagnetic region, where the magnetizations of sublattices are absent.

The above facts can be explained in the model of magnetic polarons in an antiferromagnetic matrix. The ferromagnetic microregion (the ferron radius) is determined by the competition between the kinetic energy of charge carriers and the exchange energy of localized spins [35]:

$$R_{pol} = a\left(\frac{\pi t}{4J_{ff}S^2}\right)^{1/5} \tag{3}$$

where a is the lattice period, J_{ff} is the exchange integral, and t is the hopping integral. Impurity electrons as a result of s-d interaction induce a non-collinear configuration of spins in the microregion. The exchange energy decreases at the heating as a result of a decrease in the correlation between the directions of neighboring spins. We represent the exchange energy $J_{ff}\ S^2 = J < S_0S_1 >$ in terms of the short-range order correlator $< S_0S_1 >$, which has a kink at the magnetic phase transition temperature [43]. In the Oguchi model, the short-range order parameter [43] is.

$$< S_0S_1 >= \frac{\left((2chH_{ex}+1) - 3exp\left(-\frac{2J}{kT}\right)\right)}{\left(2chH_{ex}+1+exp\left(-\frac{2J}{kT}\right)\right)}, \tag{4}$$

where H_{ex} is the exchange field. The ferron magnetization is proportional to the volume $M\ R_{pol}^3 = \frac{A}{<S_0S_1>^{3/5}}$ and qualitatively describes the temperature behavior of the residual magnetization in Fig. 7 above 100

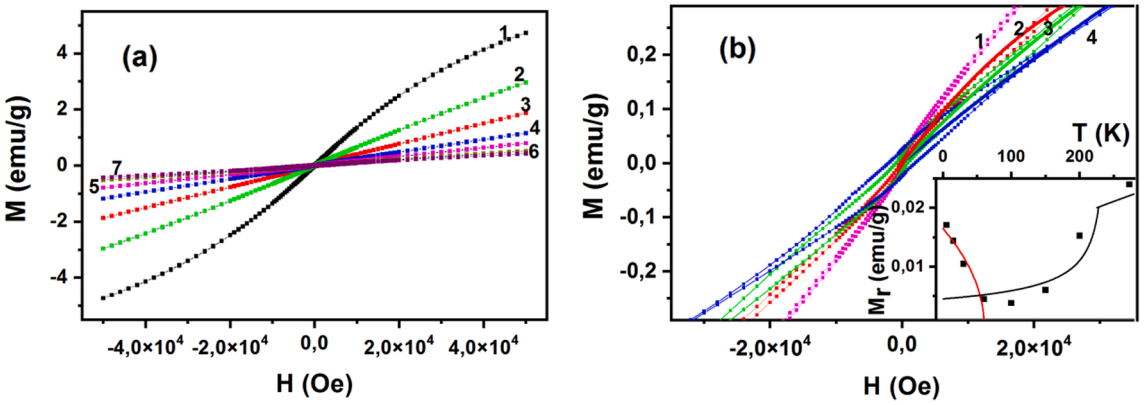

Fig. 7. The field dependence of magnetization of BSFO/BFO at different temperature: (a) Curve 1 corresponds to 5 K, 2–15 K, 3–30 K, 4–60 K, 5–100 K, 6–200 K, 7–273 K. (b) The field dependence of hysteresis magnetization. Curve 1 corresponds to 100 K, 2–150 K, 3–200 K, 4–273 K. Solid lines 2, 3, 4 show the theoretical calculations according to expression (5) at temperatures 150, 200, 273 K. Inset (b): the temperature dependence of remanence of magnetization. Experimental data are represented by symbols (squares).The theoretical calculations $M = \frac{A}{<S_0S_1>^{3/5}}$ according to expression (4) by solid line and $M_r = M_{r0}(1 - T/T_c)^{0.5}$ (dashed line).

K with fitting parameter A = 4.5 10-3. The M(H) dependences can also be explained in the model of magnetic polarons.

In the low-temperature region, according to the neutron diffraction data, a noncollinear arrangement of spins is carried out in the $Bi_2Fe_4O_9$ single crystal [44]. The noncollinear structure is formed on the pentagonal lattice in the *ab* plane with three competing exchange couplings. Oxygen atoms in each pentagon form a smaller pentagon directed opposite to the main pentagon. The positioning of oxygen atoms plays a decisive role in the difference between the values of exchange couplings and determines the degree of frustration [44]. Let us assume that, below $T_c = 60$ K, a noncollinear arrangement of the sublattices with a weak ferromagnetic moment of $M_{r0} = 0.018$ emu/g is formed in mullite. In the molecular field approximation, the magnetization is described by the power function $M_r = M_{r0}(1 - T/T_c)^{0.5}$. This model satisfactorily describes the experimental data.

3.3. Polarization

The presence of anion vacancies and electron diffusion will induce the migration-type electric polarization. Fig. 8 shows field dependences of the electric polarization in the temperature range of 80–450 K. We can distinguish two intervals: 80–200 K, where the width of the hysteresis decreases, and 240–450 K, where the remanence polarization grows exponentially. It can be assumed that the polarization in mullite below the Néel temperature is caused by a lone electron pair on the bismuth ion and the asymmetric arrangement of the nearest oxygen ions as a result of the electron density redistribution on Bi-O-Fe. The dipole-induced spontaneous polarization decreases according to the power law $P_r = P_{r0}(1 - T/T_N)^{1/2}$ and is consistent with the experimental data: $P_{r0} = 6.2$ nC/cm^2 (insert Fig. 8b). The remanence polarization P_{r0} in zero field is related to stannate and mullite. In particular, in the $Bi_2(Sn_{1-x}Fe_x)_2O_7$ compound, the polarization increases from $P_r = 1$ nC/cm^2 to 1.5 nC/cm^2 at $\times = 0.2$ and from $P_r = 3$ nC/cm^2 to 9 nC/cm^2 in BSFO/BFO upon heating from 200 to 280 K. The growth of the iron concentration will lead to an increase of the bismuth pyrostannate polarization: P_r (x = 0.3)/P_r (x = 0.2) ~ 1.5–2. The threefold increase of the composite polarization is caused by mullite. Under the action of an external electric field, carriers diffuse toward dislocations, boundaries of the crystalline phases, and crystallite surface. Here, the space charge is accumulated, which leads to an increase of the electric polarization hysteresis loop width. This polarization mechanism is defined as migration.

The hysteresis and induced polarization were calculated using the following model. On the crystallite surface, the electric charge $Q = eN$ is induced, where e is the elementary charge and N is the number of electrons transferred from the bulk. The sample polarization P = Q/S can be written as:

$$P = \int j dt = \int (\sigma_0 E) dt = \int (en\mu E) dt = \int (en\mu E_0 \sin\omega t) dt = en\mu \frac{\sqrt{E_0^2 - E^2}}{\omega}, \quad (5)$$

where μ is the carrier mobility inside a crystallite and n is the free carrier density. The hysteresis width $\Delta P = 2en\mu E_0/\omega$ is determined by the carrier density and mobility, as well as by the external field amplitude E_0. We take into account the contribution of localized charges to the polarization as $P = \varepsilon_0 \chi E$. The resulting polarization is:

$$P = \frac{en\mu\sqrt{E_0^2 - E^2}}{\omega} + \varepsilon_0 \chi E \quad (6)$$

Expression (6) satisfactorily describes the experimental data with the conductivity $\sigma = en\mu = (1–6)10^{-13}$ Ω^{-1} cm^{-1} and $\chi \approx 15$. The temperature dependence of the remanence polarization at T > 200 K is determined by the charge carrier density $n = A\exp(-\Delta E/kT)$ at the chemical potential, which increases upon heating as a result of the absorption of optical phonons $N_{ph} = 1/(1 + \exp(\omega_m/kT))$. Electrons localized near anion vacancies absorb the optical phonon of the B_{1g} mode related to the vibrations of oxygen vacancies in the *yz* plane. In $Bi_2Fe_4O_9$ and $Bi_2(Sn_{0.8}Fe_{0.2})_2O_7$, the mode frequencies are $\omega_m = 834$ cm^{-1} [19] and $\omega_{st} = 842$ cm^{-1}, [45] respectively, which is consistent with an activation energy $\Delta E_1 = 0.105(8)$ eV = 840(60) cm^{-1} determined in the range of 240–320 K. At T > 360 K, bismuth pyrostannate transforms from the α to β phase and the activation energy $\Delta E_2 = 0.22(4)$ eV = 1760(30) cm^{-1} is determined by the $^2A_{2g}(12)$ mode with a frequency of $\omega_m = 1638$ cm^{-1} [19] in mullite and $\omega_{st} = 1714$ cm^{-1} in bismuth pyrostannate. At high temperatures, the polarization is mainly determined by bismuth stannate. In the vicinity of the Néel temperature, there are two contributions: dipole and migration. The sum of the two polarization types yields a minimum at T_N and satisfactorily describes the $P_r(T)$ curve (Fig. 8b).

In the polycrystalline $Bi_2Fe_4O_9$ compound, the effect of the grain size on the electrical and ferroelectric properties was observed [25]. A remanence polarization of $P_r = 50$ nC/cm^2 was found in the $Bi_2Fe_4O_9$ composite with a grain size of 900 nm in fields of 0–15 kV/cm. Depending on a synthesis technique used, the critical grain size was found at which the electric polarization hysteresis vanishes. The ferroelectric behavior at room temperature was observed also in single-crystal $Bi_2Fe_4O_9$ nanotubes with a remanence polarization of 0.02 μC/cm^2 [46]. The ferroelectric hysteresis is attributed to the stoichiometric activity of Bi 6 s electrons.

3.4. Impedance and permittivity

The information about the magnetic or ferroelectric transition can be obtained using impedance spectroscopy. Fig. 9a presents the temperature dependence of the BSFO/BFO impedance at 10 and 100 kHz. The impedance has a jump at T = 237 K, which is independent of frequency. This temperature coincides with the Néel temperature $T_N = 237$ K. The permittivity has no anomalies around T_N (Fig. 10). The impedance consists of the active and reactive parts and, since the capacitance remains almost invariable, the jumps are related to the ac resistance. In

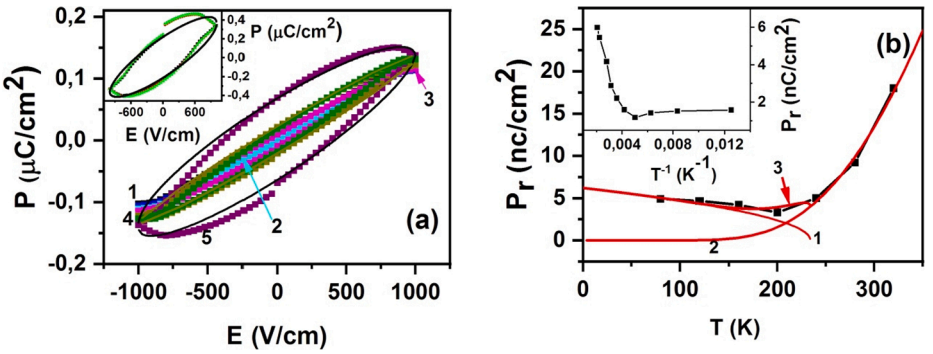

Fig. 8. (a) The field dependence of electric polarization of BSFO/BFO in magnetic field H = 12 kOe. Curve 1 corresponds to 200 K, 2–240 K, 3–280 K, 4–320 K, 5–360 K. The solid line corresponds to the theoretical calculations of expression (6). Inset corresponds to the field dependence of electric polarization of BSFO/BFO in magnetic field H = 12 kOe and T = 450 K. The solid line corresponds to the theoretical calculations of expression (6). (b) The temperature dependence of remanence of electric polarization of BSFO/BFO (squares). Curve 1 corresponds to expressions $P_r = P_{r0}(1 - T/T_N)^{1/2}$, $P_{r0} = 6.2$ nC/cm^2, $T_N = 234$ K. Curve 2 corresponds to the exponential law $P_r = B\exp(-\Delta E/kT)$, $\Delta E = 0.105$ eV. Curve 3 corresponds to the sum of two contributions from curves 1 and 2. Inset: remanence electric polarization of BSFO/BFO versus reverse temperature.

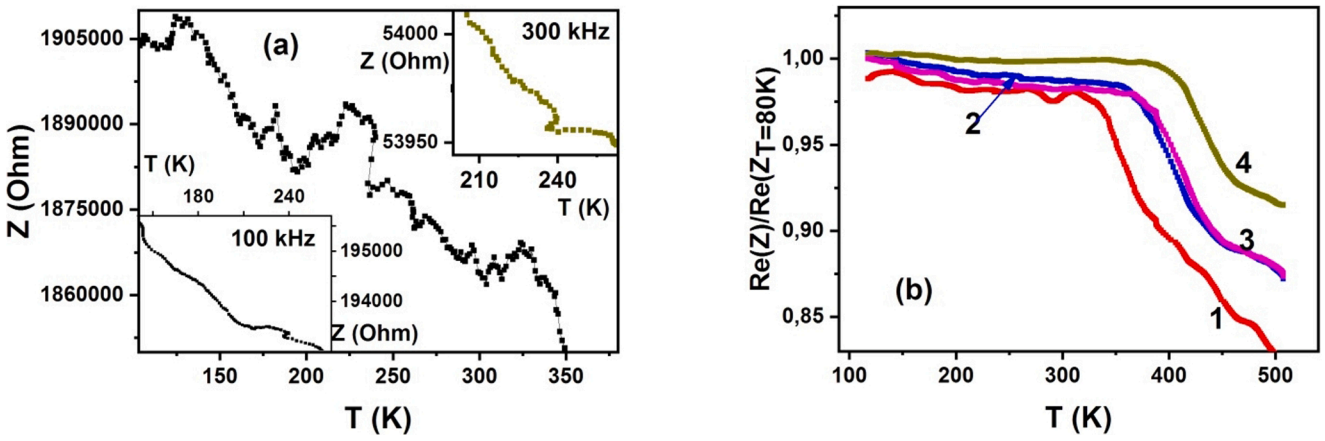

Fig. 9. (a) The temperature dependence of impedance of BSFO/BFO at 10 kHz. Insets correspond to the temperature dependence of impedance of BSFO/BFO at 100 and 300 kHz. (b) The temperature dependence of reduced impedance of BSFO/BFO. Curve 1 corresponds to 5 kHz, 2–50 kHz, 3–100 kHz, 4–300 kHz.

magnetic semiconductors, a sharp change of the resistance 1/R dR/dT in the region of the magnetic phase transition is caused by the spin polaron-type conductivity, which is confirmed by the polaron (ferron) mechanism of the hysteresis formation in mullite.

The broad permittivity maxima in the temperature range of 295–305 K are related to the destruction of the charge order induced by divalent iron ions. The temperature of the maximum of permeability depends from the frequency ω_m. In the Debye model, the relaxation time is associated with the relation: $\omega_m\tau = 1$. Using the frequency dependence of the temperatures of maxima $\varepsilon_{max}(T)$, we found the activation energy $\Delta E = 2.0(1)$ eV and the relaxation time $\tau = \tau_0 \exp(\Delta E/kT)$ (Fig. 10b). The activation energy corresponds to the electronic transition $^6A_{1g}$ - $^4T_{1g}$ in the crystal field of the $Bi_2Fe_4O_9$ octahedron [19]. For divalent iron ions, the transition will be inverted: $^4T_{1g}$ - $^6A_{1g}$. Upon heating above 300 K, the splitting T_{1g} of Fe^{2+} ions vanish. The Fe^{2+} ions found in the $Bi_2Fe_4O_9$ thin films [47] strengthen the weak ferromagnetic properties as compared with those of the bulk sample.

The jump in the Z(T) impedance at T = 140 K is caused by a phase transition occurring in bismuth pyrostannate with a decrease in the crystal symmetry [36]. A sharp decrease in the impedance with increasing temperature (T > 330 K) is consistent with an increase in the permittivity at the corresponding frequencies and results from the $\alpha \rightarrow \beta$ transition. These temperatures agree with the temperatures established previously for the $Bi_2(Sn_{0.8}Fe_{0.2})_2O_7$ compound [16].

4. Conclusions

The effect of the sample prehistory on the magnetic susceptibility of the BSFO/BFO composite and its growth upon cooling in a magnetic field was established. The previously unknown temperature dependences of the magnetic hysteresis and remanent magnetization and the absence of magnetization saturation in mullite were determined. The nonlinear field dependence of the magnetization in an antiferromagnet and the magnetic hysteresis is related to formation of ferrons. The impedance jump at the Néel temperature in mullite caused by the spin polaron-type conductivity was discovered. The temperature of formation of the noncollinear arrangement of the sublattice magnetic moments at low temperatures as a result of frustration of the exchange couplings was found.

The temperature dependence of the electric polarization and hysteresis of polarization in the BSFO/BFO composite was established, including the contribution of mullite to the electric polarization. The dipole-type electric polarization below the Néel temperature and the migration polarization at $T > T_N$ were found. It was shown that the remanent polarization is described by the the current carrier density on the chemical potential as a results of the absorption of the B_{1g} phonon mode related to the vibration of oxygen ions in the *yz* plane and with the $^2A_{2g}$ mode (12) in the bismuth stannate β phase.

Thus, the remanent magnetization of mullite in the oxygen-deficient matrix is higher than the magnetization of polycrystalline $Bi_2Fe_4O_9$ by an order of magnitude.

CRediT authorship contribution statement

S.S. Aplesnin: Conceptualization, Methodology, Writing – review & editing. **L.V. Udod:** Investigation, Writing – original draft, Writing – original draft. **M.N. Sitnikov:** Investigation. **D.A. Velikanov:** Investigation. **M.N. Molokeev:** Investigation, Writing – original draft. **O.B.**

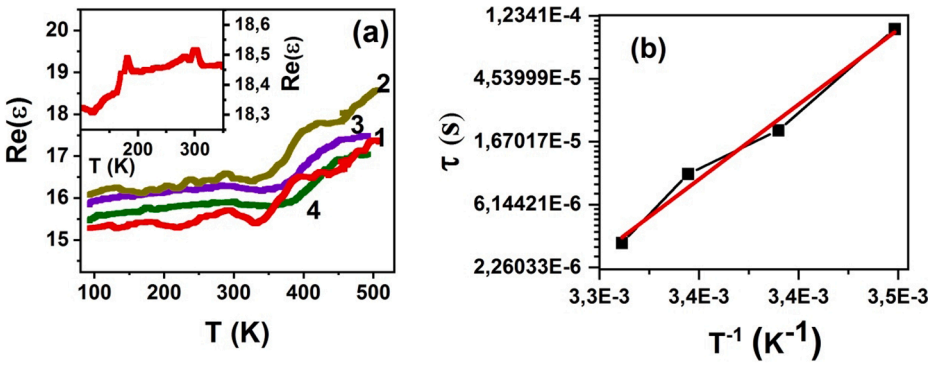

Fig. 10. (a) The temperature dependence of real part of permittivity of BSFO/BFO at different frequencies: curve 1 corresponds to 5 kHz, 2–10 kHz, 3–50 kHz, 4–100 kHz. Inset: the temperature dependence of permittivity of BSFO/BFO at 300 kHz. (b) Relaxation time for the BSFO/BFO.

Romanova: Investigation. **A.V. Shabanov:** Investigation.

Declaration of Competing Interest

The authors declare that they have no known competing financial interests or personal relationships that could have appeared to influence the work reported in this paper.

References

[1] A.S. Poghossian, H.V. Abovian, P.B. Avakian, S.H. Mkrtchian, V.M. Haroutunian, Bismuth ferrites: New materials for semiconductor gas sensors, Sens. Actuators, B 4 (3-4) (1991) 545–549.

[2] Q.-J. Ruan, W.-D. Zhang, Tunable Morphology of Bi 2 Fe 4 O 9 Crystals for Photocatalytic Oxidation, J. Phys. Chem. C 113 (10) (2009) 4168–4173.

[3] Q. Zhang, W.J. Gong, J.H. Gong, X.K. Ning, Z. H. Wang, X.G. Zhao, W. Ren, Z. Zhang, Size-dependant magnetic, photoabsorbing and photocatalytic properties of single-crystalline $Bi_2Fe_4O_9$ semiconductor nanocrystals.J. Phys. Chem. C, 115 (2011) 25241-25246. https://DOI: 10.1021/Jp208750n.

[4] I. Bloom, M.C. Hash, J.P. Zebrowski, K.M. Myles, M. Krumpelt, Oxide-ion conductivity of bismuth aluminates, Solid State Ionics 53–56 (1992) 739–747, https://doi.org/10.1016/0167-2738(92)90249-O.

[5] S. Sun, W. Wang, L. Zhang, M. Shang, Visible Light-Induced Photocatalytic Oxidation of Phenol and Aqueous Ammonia in Flowerlike Bi2Fe4O9 Suspensions, J. Phys. Chem. C 113 (29) (2009) 12826–12831.

[6] Y.i. Liu, R. Zuo, Morphology and optical absorption of $Bi_2Fe_4O_9$ crystals via mineralizer-assisted hydrothermal synthesis, Particuology 11 (5) (2013) 581–587.

[7] N.A. Spaldin, S.-W. Cheong, R. Ramesh, Multiferroics: past, present, and future, Phys. Today 63 (10) (2010) 38–43, https://doi.org/10.1063/1.3502547.

[8] X.L. Zhong, J.B. Wang, M. Liao, G.J. Huang, S.H. Xie, Y.C. Zhou, Y. Qiao, J.P. He, Multiferroic nanoparticulate $Bi_{3.15}Nd_{0.85}Ti_3O_{12}$–$CoFe_2O_4$ composite thin films prepared by a chemical solution deposition technique, Appl. Phys. Lett. 90 (15) (2007) 152903, https://doi.org/10.1063/1.2709946.

[9] D.A. Sánchez, N. Ortega, A. Kumar, R. Roque-Malherbe, R. Polanco, J.F. Scott, R. S. Katiyar, Symmetries and multiferroic properties of new room-temperature magnetoelectrics: lead iron tantalate—lead zirconate titanate (PFT/PZT), AIP Adv. 1 (2011), 042169, https://doi.org/10.1063/1.3670361.

[10] N. Ortega, A. Kumar, J.F. Scott, R.S. Katiyar, Multifunctional magnetoelectric materials for device applications, J. Phys.: Condens. Matter 27 (50) (2015) 504002, https://doi.org/10.1088/0953-8984/27/50/504002.

[11] J. Ma, J. Hu, Z. Li, and C.-W. Nan, Recent Progress in Multiferroic Magnetoelectric Composites: from Bulk to Thin Films, Adv. Mater., 23 (2011) 1062–1087. https://DOI: 10.1002/adma.201190024.

[12] S.S. Aplesnin, L.V. Udod, M.N. Sitnikov, N.P. Shestakov, $Bi_2(Sn_{0.95}Cr_{0.05})_2O_7$: Structure, IR spectra, and dielectric properties, Ceram. Int. 42 (2016) 5177–5183, https://doi.org/10.1016/j.ceramint.2015.12.040.

[13] S.S. Aplesnin, L.V. Udod, M.N. Sitnikov, V.V. Kretinin, M.S. Molokeev, N. Mironova-Ulmane, Dipole glass in chromium-substituted bismuth pyrostannate, Mater. Res. Express 5 (11) (2018) 115202, https://doi.org/10.1088/2053-1591/aaddd9.

[14] S.S. Aplesnin, L.V. Udod, M.N. Sitnikov, E.V. Eremin, M.S. Molokeev, L. S. Tarasova, K.I. Yanushkevich, A.I. Galyas, Correlation of the magnetic and transport properties with polymorphic transitions in bismuth pyrostannate Bi2(Sn1 − x Cr x)2O7, Phys. Solid State 57 (8) (2015) 1627–1632.

[15] S.S. Aplesnin, L.V. Udod, M.N. Sitnikov, Electronic transition, ferroelectric and thermoelectric properties of bismuth pyrostannate $Bi_2(Sn_{0.85}Cr_{0.15})_2O_7$, Ceram. Int. 44 (2) (2018) 1614–1620, https://doi.org/10.1016/j.ceramint.2017.10.082.

[16] L. Udod, S. Aplesnin, M. Sitnikov, O. Romanova, O. Bayukov, A. Vorotinov, D. Velikanov, G. Patrin, Magnetodielectric effect and spin state of iron ions in iron-substituted bismuth pyrostannate, EPJP 135 (2020) 776, https://doi.org/10.1140/epjp/s13360-020-00781-2.

[17] S.S. Aplesnin, L.V. Udod, M.N. Sitnikov, O.B. Romanova, Dielectric and transport properties, electric polarization at the sequential structural phase transitions in iron-substituted bismuth pyrostannate, Ceram. Int. 47 (2) (2021) 1704–1711, https://doi.org/10.1016/j.ceramint.2020.08.287.

[18] J. Allibe, S. Fusil, K. Bouzehouane, C. Daumont, D. Sando, E. Jacquet, C. Deranlot, M. Bibes, A. Barthélémy, Room Temperature Electrical Manipulation of Giant Magnetoresistance in Spin Valves Exchange-Biased with BiFeO 3, Nano Lett. 12 (3) (2012) 1141–1145.

[19] M.N. Iliev, A.P. Litvinchuk, V.G. Hadjiev, M.M. Gospodinov, V. Skumryev, E. Ressouche, Phonon and magnon scattering of antiferromagnetic $Bi_2Fe_4O_9$, Phys. Rev. B, 81 (2010) 024302(8). https://DOI: 10.1103/PhysRevB.81.024302.

[20] N. Shamir, E. Gurewitz, H. Shaked, The magnetic structure of $Bi_2Fe_4O_9$ – analysis of neutron diffraction measurements, Acta Crystallogr. A 34 (1978) 662–666.

[21] Z. Pchelkina, S. Streltsov, Ab initio investigation of the exchange interactions in $Bi_2Fe_4O_9$: the Cairo pentagonal lattice compound Phys, Rev. B 88 (2013), 054424, https://doi.org/10.1103/PhysRevB.88.054424.

[22] J. Zhao, T. Liu, Y. Xu, Y. He, W. Chen, Synthesis and characterization of $Bi_2Fe_4O_9$ powders, Mater. Chem. Phys. 128 (2011) 388–391, https://doi.org/10.1016/j.matchemphys.2011.03.011.

[23] G. Alvarez, J. Contreras, A. Conde-Gallardo, H. Montiel, R. Zamorano, Detection of para–antiferromagnetic transition in $Bi_2Fe_4O_9$ powders by means of microwave absorption measurements, J. Magn. Magn Mater. 348 (2013) 17–21, https://doi.org/10.1016/j.jmmm.2013.08.014.

[24] G.C. Papaefthymiou, A.J. Viescas, J.-M. Le Breton, H. Chiron, J. Juraszek, T.-J. Park, S.S. Wong, Magnetic and Mössbauer characterization of the magnetic properties of single-crystalline sub-micron sized $Bi_2Fe_4O_9$ cubes, Curr. Appl Phys. 15 (3) (2015) 417–422.

[25] Z.M. Tian, S.L. Yuan, X.L. Wang, X.F. Zheng, S.Y. Yin, C.H. Wang, L. Liu, Size effect on magnetic and ferroelectric properties in $Bi_2Fe_4O_9$ multiferroic ceramics, J. Appl. Phys. 106 (10) (2009) 103912, https://doi.org/10.1063/1.3259392.

[26] A.A. Zatyupo, L.A. Bashkirov, I.O. Troyanchuk, G.S. Petrov, A.I. Galyas, L.S. Lobanovsky, S.V. Trukhanov, I.M. Sirota, Magnetization, magnetic susceptibility, effective magnetic moment of Fe^{3+} ions in ferit $Bi_2Fe_4O_9$, Inorg. Mat. 49 (2013) 658-662. https://Doi: 10.7868/S0002337X13060201.

[27] X. Wu, J. Miao, Y. Zhao, X. Meng, X. Xu, S. Wang, Y. Jiang, Novel multiferroic $Bi_2Fe_4O_9$ nanoparticles: the interesting optical, photocatalytic, and multiferroic properties, Optoelectron Adv. Mater.-RAPID Commun. 7 (2013) 116–120.

[28] A.K. Singh, S.D. Kaushik, B. Kumar, P.K. Mishra, A. Venimadhav, V. Siruguri, S. Patnaik, Substantial magneto-electric coupling near room temperature in $Bi_2Fe_4O_9$, Appl. Phys. Lett. 92 (13) (2008) 132910, https://doi.org/10.1063/1.2905815.

[29] P. D. Borges, L. M. R. Scolfaro, H. W. L. Alves, E. F. Jr. Silva, L. V. C. Assali, Study of the oxygen vacancy influence on magnetic properties of Fe- and Co-doped SnO_2 diluted alloys, NRL, 7 (2012) 540. https://doi.org/10.1186/1556-276X-7-540.

[30] M. Zhou, Y. Wang, Y. Zhang, L.i. Sun, W. Hao, E. Cao, Z. Yang, Effects of oxygen vacancy on the magnetic properties of Mn(II)-doped anatase TiO_2, Chem. Phys. Lett. 754 (2020) 137738, https://doi.org/10.1016/j.cplett.2020.137738.

[31] E. Cho, K. Klyukin, S. Ning, J. Li, R. Comin, R.J. Green, B. Yildiz, C.A. Ross, First-principles calculation of oxygen vacancy effects on the magnetic properties of the perovskite $SrNiO_3$, Phys. Rev. Materials 5 (2021), 094413, https://doi.org/10.1103/PhysRevMaterials.5.094413.

[32] M. Hoffmann, V.N. Antonov, L.V. Bekenov, K. Kokko, W. Hergert, A. Ernst, Variation of magnetic properties of Sr_2FeMoO_6 due to oxygen vacancies, J. Phys.: Condens. Matter 30 (30) (2018) 305801, https://doi.org/10.1088/1361-648X/aacb8d.

[33] C. Menéndez, D. Chu, C. Cazorla, Oxygen-vacancy induced magnetic phase transitions in multiferroic thin films, npj Comput Mater 6 (2020) 76, https://doi.org/10.1038/s41524-020-0344-3.

[34] E.L. Nagaev, Lanthanum manganites and other magnetic conductors with giant magnetoresistance, UFN 166 (1996) 833–853, in russ.

[35] M. Yu. Kagan, K. I. Kugel, Inhomogeneous charge states and phase separation in manganites, UFN, 171 (2001) 577–596 (in russ). https://doi.org/10.3367/UFNr.0171.200106a.0577.

[36] B.J. Kennedy, Oxygen Vacancies in Pyrochlore Oxides: Powder Neutron Diffraction Study of $Pb_2Ir_2O_{6.5}$ and $Bi_2Ir_2O_{7-y}$, J. Solid State Cem. 123 (1) (1996) 14–20, https://doi.org/10.1006/jssc.1996.0146.

[37] I.R. Evans, J.A.K. Howard, J.S.O. Evans, α-Bi 2 Sn 2 O 7 – a 176 atom crystal structure from powder diffraction data, J. Mater. Chem. 13 (9) (2003) 2098–2103.

[38] M.K. Verma, V. Kumar, T. Das, R.K. Sonwani, V.S. Rai, D. Prajapati, K. Sahoo, V.K. Kushwaha, A. Gupta, K. Mandal, Synthesis of $Bi_2Fe_4O_9$ Crystalline Ceramic as Extremely Capable Photocatalyst via Proficient Chemical Route, J. Miner. Mater Char Eng., 9 (2021) 444-461. https://DOI: 10.4236/jmmce.2021.95030.

[39] Bruker AXS TOPAS V4:General profile and structure analysis software for powder diffraction data. – User's Manual. Bruker AXS, Karlsruhe, Germany. 2008.

[40] J.-T. Han, Y.-H. Huang, R.-J. Jia, G.-C. Shan, R.-Q. Guo, W. Huang, Synthesis and magnetic property of submicron $Bi_2Fe_4O_9$, J. Cryst. Growth 294 (2006) 469–473, https://doi.org/10.1016/j.jcrysgro.2006.07.006.

[41] M. Pooladi, I. Sharifi, M. Behzadipour, A review of the structure, magnetic and electrical properties of bismuth ferrite ($Bi_2Fe_4O_9$), Ceram. Int. 46 (11) (2020) 18453–18463, https://doi.org/10.1016/j.ceramint.2020.04.241.

[42] D.P. Dutta, C. Sudakar, P.S.V. Mocherla, B.P. Mandal, O.D. Jayakumar, A.K. Tyagi, Enhanced magnetic and ferroelectric properties in scandium doped nano $Bi_2Fe_4O_9$, Mater. Chem. Phys. 135 (2-3) (2012) 998–1004.

[43] J S. Smart, Effective Field Theories of Magnetism, W B Saunders company, Philadelphia- London, 1966, -271 p.

[44] E. Ressouche, V. Simonet, B. Canals, M. Gospodinov, V. Skumryev, Magnetic Frustration in an Iron-Based Cairo Pentagonal Lattice, Phys. Rev. Lett. 103 (26) (2009), https://doi.org/10.1103/PhysRevLett.103.267204.

[45] L.V. Udod, S.S. Aplesnin, M.N. Sitnikov, O.B. Romanova, M.N. Molokeev, Phase transitions in bismuth pyrostannate upon substitution of tin by iron ions, J. Alloys Comp. 804 (2019) 281–287, https://doi.org/10.1016/j.jallcom.2019.07.020.

[46] P. Hajra, R.P. Maiti, D. Chakravorty, Room temperature magnetoelectric coupling in single crystal $Bi_2Fe_4O_9$ nanotubes grown within an anodic aluminum oxide template, Mater. Lett. 81 (2012) 138–141.

[47] H. Sun, X. Lu, T. Xu, J. Su, Y. Jin, C. Ju, F. Huang, J. Zhu, Study of multiferroic properties in Bi5Fe0.5Co0.5Ti3O15 thin films, J. Appl. Phys. 111 (12) (2012) 124116, https://doi.org/10.1063/1.4730892.